Available online at www.sciencedirect.com
SCIENCE DIRECT®
Journal of Catalysis 221 (2004) 386–399
JOURNAL OF CATALYSIS
www.elsevier.com/locate/jcat

# Catalyst support effects in the growth of structured carbon from the decomposition of ethylene over nickel

Colin Park [1] and Mark A. Keane *

*Department of Chemical and Materials Engineering, University of Kentucky, Lexington, KY 40506-0046, USA*

Received 26 June 2003; revised 21 August 2003; accepted 22 August 2003

**Abstract**

The characteristics of carbon nanofibers generated during ethylene decomposition over supported nickel can be readily manipulated by a judicious choice of the support material. The occurrence and ramifications of Ni/support interaction(s), in terms of Ni particle size/morphology/orientation, are considered and related to the carbon structure/dimensions and yield. A $7 \pm 1\%$ w/w Ni loading was achieved by standard impregnation of $SiO_2$, $Al_2O_3$, MgO, $Ta_2O_5$, activated carbon (AC), and graphite: the reduced catalysts have been characterized by $H_2$ chemisorption, CO chemisorption/temperature-programmed desorption (TPD), and high-resolution transmission electron microscopy (HRTEM). The reaction of ethylene with hydrogen over these catalysts also generated ethane via hydrogenation, a step that was favored over $Ni/Al_2O_3$ and Ni/MgO. Carbon yield (where $T < 800$ K) increased in the sequence $Ni/Al_2O_3 \sim Ni/MgO < Ni/AC < Ni/graphite < Ni/Ta_2O_5 < Ni/SiO_2$; at higher temperatures ($> 850$ K), Ni/AC and Ni/graphite delivered the highest yields. With the exception of Ni/graphite and $Ni/Ta_2O_5$, which produced helical and highly curved fibers, the other supported Ni catalysts generated a relatively straight (limited curvature) fibrous growth. The occurrence of Ni fragmentation and secondary fiber growth from such fragments is illustrated and discussed. The influence of $H_2$ content in the feed was investigated with respect to both carbon yield and structure; an increased $H_2$ content served to enhance fiber structural order. Temperature-programmed oxidation studies have been used to probe the graphitic nature of the carbon product; the results are consistent with HRTEM analysis.


*Keywords:* Carbon nanofibers; Ethylene decomposition; Supported nickel

## 1. Introduction

Modification to the properties of supported metals through the choice of substrate is not a new concept. As early as the 1930s it was recognized that the presence of highly charged cations on an oxide surface altered the catalytic properties of supported metals [1]. The use of a support to disperse a chosen metal is not only of economic benefit (lower preparation costs/longer productive lifetime) but the substrate can also influence catalyst performance through electronic interaction(s), spillover, and migration effects [2–5]. Electronic perturbation is most aptly demonstrated in the case of $TiO_2$ [6,7], leading to dramatic changes in the chemisorptive capacity of Pt, Rh, Pd, and Ir [8]. The impact on chemisorption also extends to Fe, Ni, and Co but the consensus of opinion is that higher reduction temperatures are needed to induce "strong metal/support interactions" (SMSI) with these metals [9–11]. Since the pioneering work on SMSI dating from the late 1970s [8,12], the use of supports to induce changes in the catalytic behavior of dispersed metals has been the subject of a number of reports [4,6,7,13,14].

The generation of ordered carbonaceous structures (fullerenes, nanotubes, and nanofibers) is a burgeoning area of catalysis research [15–20]. The unique chemical and physical properties associated with carbon nanofibers, the focus of this study, can be put to good effect in diverse applications, i.e., as catalyst supports [13,16,21–23], polymer reinforcement agents [24], fuel cell electrodes [25], adsorbents [26], and in energy storage [18]. Carbon nanofibers can be readily generated from mono- and bimetallic catalysts via the decomposition ($723 \text{ K} \leqslant T \leqslant 923$ K) of a range of carbon-containing compounds [16,20,27,28]. There is ample evi-

* Corresponding author.
*E-mail address:* makeane@engr.uky.edu (M.A. Keane).
[1] Current address: Synetix, P.O. Box 1, Belasis Avenue, Billingham, Cleveland, TS23 1LB, UK.

0021-9517/$ – see front matter 
doi:10.1016/j.jcat.2003.08.014

dence to show that the dimensions/lattice orientations of the carbon product are governed by the dimensions/electronic structure of the catalytic metal particles [16,29]. Use of non-supported metal(s) can generate significant carbon yields (up to 250 $g_C/g_{cat}$) but there is little or no control over the diameter of the nanofiber [16,20,28]. One way to address this failing is through the use of supported catalysts bearing smaller metal particles that promote the growth of narrower and more uniformly sized fibers [30,31]. A drawback to this approach has been the relatively low yields of carbon (up to 2 $g_C/g_{cat}$) that have been typically produced [31–35]. It should, however, be noted that Avdeeva and co-workers, using coprecipitated Ni–alumina, have recorded carbon yields (up to 250 $g_C/g_{cat}$) similar to those generated by metallic powders [36,37].

In a recent study [30], we evaluated the application of Ni supported on Y zeolite and silica for the controlled growth of ordered carbon nanofibers. While carbon production was limited by the interconnecting microporous network of the zeolite, the carbon morphology/structure was similar for both Ni/zeolite and Ni/$SiO_2$, albeit a sharper distribution of narrower fibers was generated from the Ni-impregnated zeolite. A search through the literature has failed to unearth a comprehensive examination of the role of the support in carbon growth from Ni. The published studies have largely been focused on the use of $SiO_2$, $Al_2O_3$, and graphite to support a variety of metals [24,31–36,38,39]. In this paper, we examine the role that Ni/support interaction(s) can play in the catalytic decomposition of ethylene to carbon. An intentional inducement of electronic perturbations in the dispersed Ni by varying the nature of the support should impact on carbon fiber dimensions and/or morphology and/or lattice structure; control of such effects is the premise on which this work is based. We have considered an array of substrates, ranging from a basic MgO to conventional $Al_2O_3$ and $SiO_2$, as well as $Ta_2O_5$, a highly refractive oxide that exhibits many of the qualities of $TiO_2$ [12,40]. The use of graphite, a material known [38] to induce SMSI, and a high surface area activated carbon (AC) with little or no metal/support interaction have also been investigated.

## 2. Experimental

### 2.1. Catalyst preparation, activation, and characterization

The $SiO_2$ (fumed), $Al_2O_3$, $Ta_2O_5$, and MgO substrates were supplied by Sigma-Aldrich and used as received. The activated carbon (G-60, 100 mesh) was obtained from NORIT (UK) and the graphite (synthetic 1–2 μm powder) from Sigma-Aldrich. Both carbonaceous materials underwent a demineralization (continuous agitation in 1 M $HNO_3$ for up to 7 days) to remove any residual metal impurities that could contribute to the catalytic step. The Ni-loaded ($7 \pm 1\%$ w/w) samples were prepared by standard incipient wetness impregnation where a 2-butanolic $Ni(NO_3)_2$ solution was added dropwise at 353 K to the substrate with constant agitation (500 rpm). Aqueous solutions were not used as the carbon support materials are hydrophobic, leading to difficulties with surface wetting that can impact on the ultimate metal dispersion [22,26,41]. The Ni content was determined (to within ±3%) by atomic absorption spectrophotometry (VarianSpectra AA-10); the samples were digested in HF (37% conc.) overnight at ambient temperature. The catalyst precursors were subsequently dried at 383 K, calcined (10 K/min) in air at 623 K, cooled to ambient temperature, and heated (10 K/min) to the ultimate reaction temperature in 20% v/v $H_2$/He. Samples for off-line TEM analysis were cooled (in He) and passivated in a 2% v/v $O_2$/He mixture at room temperature.

$H_2$ and CO chemisorption were employed to characterize the supported Ni sites where the catalyst was cooled, following the reduction step, to 298 K in dry He and a fixed volume (10 μl) of $H_2$ or CO pulsed into the He carrier gas stream; the concentration of $H_2$ or CO exiting the reactor was measured using an on-line thermal conductivity detector (TCD). The injections were repeated until the downstream peak area was constant, indicating surface saturation. A subsequent series of calibration peaks were taken at ambient temperature to quantify $H_2$ or CO uptake; reproducibility was better than ±3%. The CO-loaded catalysts were thoroughly flushed with dry He for 1 h and ramped (TPD at 25 K/min) to 1073 K with continual monitoring of the exiting gas; data acquisition and analysis were performed using the JCL 6000 (for Windows) software package. The bed temperature was continuously monitored by means of a data logging system (Pico Technology, Model TC-08) to give an accurate measure of the desorption temperature. Nitrogen BET surface area measurements were carried out at 77 K (Autosorb-1-C, Quantachrome) on freshly reduced catalysts.

### 2.2. Catalytic carbon growth procedure/carbon characterization

All catalytic reactions were carried out under atmospheric pressure, in situ following the activation step (and a 1 h He flush), in a fixed-bed silica reactor over the temperature range 673–898 K. The reaction temperature was monitored continuously by a thermocouple inserted in a thermowell within the catalyst bed; catalyst temperature was constant to within ±2 K. The catalytic measurements were conducted where $W/Q = 0.5\text{–}2 \times 10^{-5}$ g/(cm$^3$ h$^{-1}$): $W$ = weight of activated catalyst; $Q$ = inlet volumetric $C_2H_4$ feed rate. The overall gas hourly space velocity (GHSV) was maintained at a constant 11,300 h$^{-1}$ with a $C_2H_4/H_2$ molar ratio in the range 1/4 to 4/1. One set of reaction conditions was chosen to assess the performance of each catalyst: $C_2H_4/H_2$ = 4/1 v/v; $T$ = 773 K; $t$ = 1 h. The effluent gas was analyzed by on-line capillary chromatography using an AI Cambridge GC94 chromatograph equipped with a split/splitless injector and a flame ionization detector, employing a DB-1

50 m × 0.20 mm i.d., 0.33 μm capillary column (J&W Scientific). The gaseous stream was sampled at regular intervals by means of a heated gas-sampling valve and all interconnecting tubing was maintained at elevated temperatures. The catalyst was contacted with the $C_2H_4/H_2$ mixture for 1 h to achieve a uniform carbon growth with no appreciable pressure deviations/flow disruption. Preliminary studies [30] established that this reaction time generated a representative carbon growth that could be linked to catalyst structural characteristics in a meaningful way. The reactor was subsequently cooled to ambient temperature and the sample passivated in a 2% v/v $O_2$/He mixture before any weight changes, due to carbon deposition, was determined. Repeated (up to five) catalytic runs generated product compositions that were reproducible to better than ±7%. The yield of solid carbon ($Y_C$) was calculated using the following expression

$$Y_C = \frac{(C_2H_4)_{input} - (CH_4/2 + C_2H_4 + C_2H_6)_{output}}{(C_2H_4)_{input}}$$

and is expressed in this paper as gram C per gram catalyst (or Ni). The selectivity in terms of (say) ethane is given by

$$S_{C_2H_6}\,(\%) = \frac{Y_{C_2H_6}}{\sum (CH_4 + C + C_2H_6)_{output}} \times 100.$$

Temperature-programmed oxidation (TPO) profiles of the catalytically generated carbon were obtained from thoroughly washed, demineralized samples to avoid any possible catalyzed gasification of carbon by residual Ni. A known mass (ca. 100 mg) of a demineralized sample was ramped (25 K/min) from room temperature to 1198 K in a 5% v/v $O_2$/He mixture with on-line TCD analysis of the exhaust gas; the catalyst bed temperature was again independently monitored using the TC-08 data logger. These profiles were compared against those generated for conventional demineralized carbon systems, i.e., the graphite and amorphous carbon that served as Ni supports. All gasses (He (99.99%), $C_2H_4$ (99.95%), $H_2$ (99.99%), and 5% v/v $O_2$/He (99.9%)) were dried by passage through activated molecular sieves before use. High-resolution transmission electron microscopy (HRTEM) analysis of both the catalysts and the carbon product was carried out using a Philips CM200 FEGTEM microscope operated at an accelerating voltage of 200 kV. The specimens were prepared by ultrasonic dispersion in butan-2-ol, evaporating a drop of the resultant suspension onto a holey carbon support grid. The Ni particle (and carbon nanofiber)-size distribution profiles presented in this study are based on a measurement of over 500 individual particles/nanofibers. Analysis by scanning electron microscopy (SEM) was carried out using a Hitachi S900 field emission SEM, operated at an accelerating voltage of 25 kV; the sample was deposited on a standard aluminum SEM holder and coated with gold.

Table 1
Nickel loading, surface-weighted average Ni particle size based on CO chemisorption ($d_{CO}$), $H_2$ chemisorption ($d_H$) and TEM ($d_{TEM}$) measurements, the characteristic CO TPD $T_{max}$ values and BET surface areas associated with the six activated supported Ni catalysts

| Catalyst | Ni (%) | $d_{CO}$ (nm) | $T_{max}$ (K) | $d_H$ (nm) | $d_{TEM}$ (nm) | BET surface area ($m^2/g$) |
|---|---|---|---|---|---|---|
| $Ni/SiO_2$ | 7 | 16.3 | **935** | 8.2 | 9.6 | 203 |
| $Ni/Al_2O_3$ | 6 | 12.1 | 878, **1013** | 5.4 | 5.7 | 120 |
| Ni/AC | 6 | 28.1 | 716, **948**, 1098 | 25.8 | 23.4 | 904 |
| Ni/graphite | 8 | 84.2 | 726, **898** | 22.3 | 27.1 | 10 |
| Ni/MgO | 7 | 8.9 | 855, **925** | 8.5 | 10.5 | 105 |
| $Ni/Ta_2O_5$ | 7 | 68.4 | 703, **848** | 13.0 | 15.2 | 8 |

The $T_{max}$ values associated with the principal desorption peaks are given in bold font.

## 3. Results and discussion

### 3.1. Characterization of the activated catalysts

The Ni loading, TEM, and CO/$H_2$ chemisorption derived mean Ni particle diameters and BET surface areas for the six activated catalysts are recorded in Table 1; representative TEM images are provided in Fig. 1. The size distribution and morphology of the supported Ni particles (at a common Ni loading) are inherent features of the interfacial energies associated with each system [42]. Selected area electron diffraction (SAED) confirmed that the Ni distributed over each support was present in the metallic form and not as an oxide. Representative high-resolution TEM images are provided in the inset to Fig. 1 that illustrates the lattice structure of Ni dispersed on $SiO_2$. Graphite has a low (BET) surface area with few edge positions available for depositing the metal, which, as a direct consequence, is present in the form of large particles (up to 80 nm) at this loading [43]. Nevertheless, these particles can be seen in Fig. 1a to possess well-defined geometrical shapes, diagnostic of metal–graphite interaction [42]. Nickel particle-size distributions, derived from the TEM analysis, are presented in the histograms given in Fig. 2. It is immediately evident that Ni supported on either carbonaceous (graphite or activated carbon) substrate exhibits a significantly wider size distribution when compared with the oxide supports. Activation of Ni/MgO led to a dehydration/reduction of MgO, where the removal of lattice oxygen resulted in a reconstruction of the substrate to generate acicular needle-like magnesium oxide, visible in Fig. 1b. It has been shown elsewhere [44–46] that hydrothermal treatment of MgO generates a diversity of morphologies; the most common being lamellar or needle-like with associated defects and irregular intercrystalline channels. Reduction of the Ni-impregnated activated carbon, an essentially amorphous material with a high (BET) surface area, yielded a metal phase of dimensions comparable to that associated with Ni/graphite, albeit a narrower size range and smaller average diameter (Table 1). Growth of Ni particles in this case can be attributed to weaker metal/support interac-

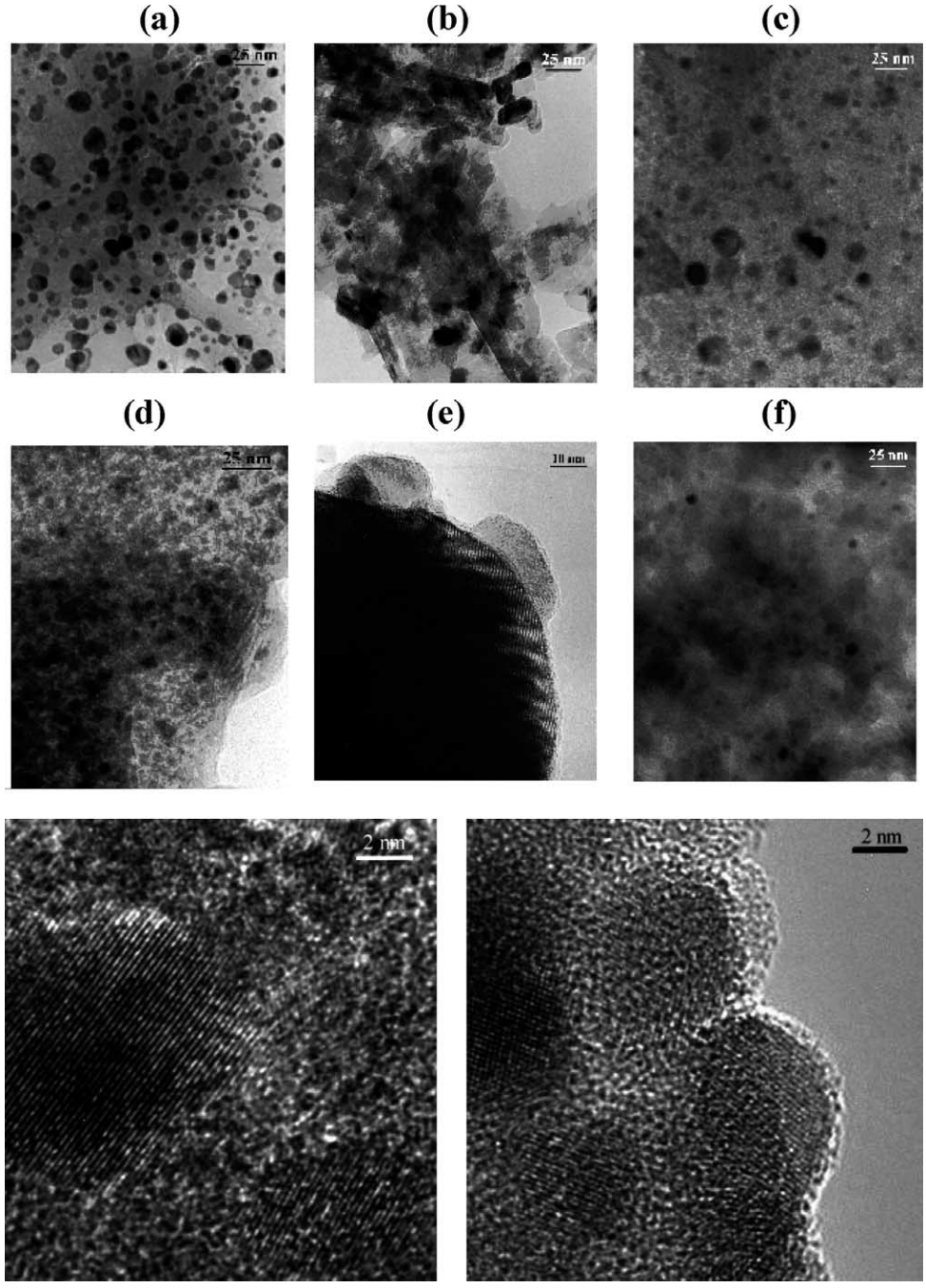


Fig. 1. Representative TEM images of activated (a) Ni/graphite, (b) Ni/MgO, (c) Ni/AC, (d) $Ni/Al_2O_3$, (e) $Ni/Ta_2O_5$, and (f) $Ni/SiO_2$. Inset at bottom, HRTEM images showing the lattice structure of Ni dispersed on $SiO_2$.

tion(s), leading to increased Ni mobility and the subsequent greater probability of agglomeration. The weaker Ni–carbon interaction is manifested in the spherical/globular nature of the Ni particles, as shown in Fig. 1c. The Ni phase associated with $Al_2O_3$ is characterized by the narrowest distribution (Fig. 2) of smaller crystallites; the nature of the metal dispersion is illustrated in Fig. 1d. The average Ni diameter was the lowest among the six supported catalysts investigated (Table 1), a feature that finds support in earlier work by Hoang-Van and co-workers [47]. The suppression of particle growth in this case has been attributed to the ionic nature of the $Ni/Al_2O_3$ interaction, leading to an enhanced dispersion of electron-deficient Ni [48]. The Ni phase on $Ta_2O_5$ is predominately "spread" along the edges of the oxide as shown in Fig. 1e, with evidence of faceting and "pill-box"-shaped particles, as reported elsewhere [49]. An exclusively spherical Ni morphology is in evidence on the $SiO_2$ support (Fig. 1f) in keeping with earlier TEM characterization reports [50,51]. Previous studies [52,53] have shown that $Ni/SiO_2$ prepared by impregnation realizes a relatively weak metal/support interaction resulting in Ni growth during activation.

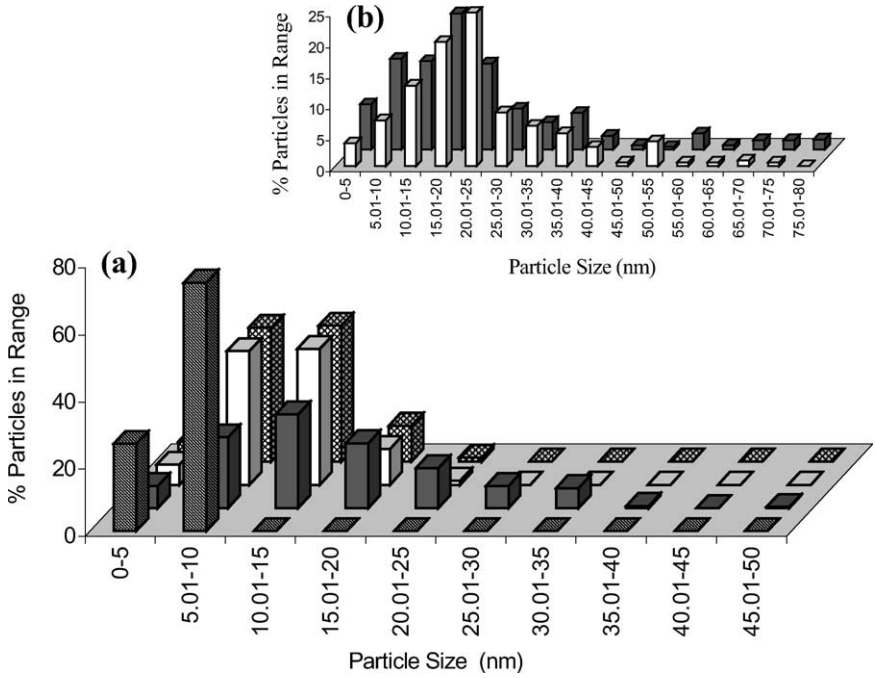


Fig. 2. (a) Ni particle-size distributions associated with freshly activated $Ni/Al_2O_3$ (downward hatched bars), $Ni/Ta_2O_5$ (solid bars), Ni/MgO (open bars), and $Ni/SiO_2$ (cross-hatched bars). (b) Inset, Ni/AC (open bars) and Ni/graphite (solid bars).

There is a decided mismatch in the Ni particle sizes derived from CO uptake values ($d_{CO}$) and TEM analysis ($d_{TEM}$), as revealed in Table 1; $d_{TEM}$ is typically lower than $d_{CO}$. Such discrepancies suggest some deviation from an exclusive 1:1 CO:Ni adsorption stoichiometry, as is normally applied, i.e., a linear single-point attachment. The surface stoichiometry is known to be dependent on metal loading and catalyst composition [54] and there have been a number of reported instances [55,56] where the dimensions of supported metal particles that are measured differ depending on the analytical technique that is employed. Moreover, the TEM approach has a decided disadvantage where insufficient contrast in the image can hamper an accurate analysis. Although there is an apparent consistency of $d_{TEM}$ and $d_{CO}$ values in the case of Ni/MgO, adsorption and subsequent dissociation of CO on the MgO are known to give unrepresentative results [57–59]. CO interaction with MgO can lead to disproportionation and/or oligomerization, generating CO uptakes with little value in terms of metal dispersion measurements [57,58,60]. The differences in $d_{TEM}$ and $d_{CO}$ are particularly pronounced in the case of $Ni/Ta_2O_5$, and Ni/graphite, suggestive of a possible suppression of CO uptake. As an addendum to the particle-size analyses, $H_2$ chemisorption was also considered and the estimated Ni sizes, based on a 2:1 adsorption stoichiometry, are given in Table 1. The agreement with the TEM results is much better, albeit $H_2$ chemisorption delivers, in the main, smaller average Ni diameters.

Notwithstanding the apparent CO uptake discrepancies, temperature-programmed desorption of CO has been used to good effect elsewhere [61–63] to probe the electronic properties of supported metal particles; the characteristic CO TPD $T_{max}$ values are recorded in Table 1. CO desorption from $Ni/SiO_2$ delivered a single characteristic peak whereas the TPD profiles associated with the other catalysts bore at least two peaks, one of which predominated. A shift in CO TPD to higher temperatures is diagnostic of stronger CO/catalyst interactions, which appear to apply to CO on $Ni/SiO_2$, $Ni/Al_2O_3$, and Ni/AC. The predominance of lower $T$ desorption of CO from Ni/graphite and $Ni/Ta_2O_5$ (and Ni/MgO to a lesser extent) is indicative of SMSI effects, i.e., weaker metal/adsorbent interaction. The latter can be linked to the anomalous Ni particle sizes generated from CO adsorption on these catalysts. While the CO chemisorption/TPD results are by no means conclusive, when considered along with $TEM/H_2$ chemisorption it is reasonable to state that the Ni phase associated with the six supports considered in this study is present in a range of sizes, morphologies, and possible electronic perturbations.

### 3.2. Carbon growth: influence of reaction temperature

The decomposition of ethylene is an attractive route to ordered carbonaceous materials as the number of possible products is limited while the carbon that is generated is typically of a high purity [64]. The structural characteristics of the carbon product can be assessed from the SEM images presented in Fig. 3, taking $Ni/SiO_2$ as a representative catalyst; the fibrous nature of the carbon growth is immediately evident. The principal competing reaction is hydrogenation to ethane while hydrogenolysis to methane occurs to a lesser extent; trace amounts of $C_3$ and $C_4$ products were also detected. Methane was only isolated in the

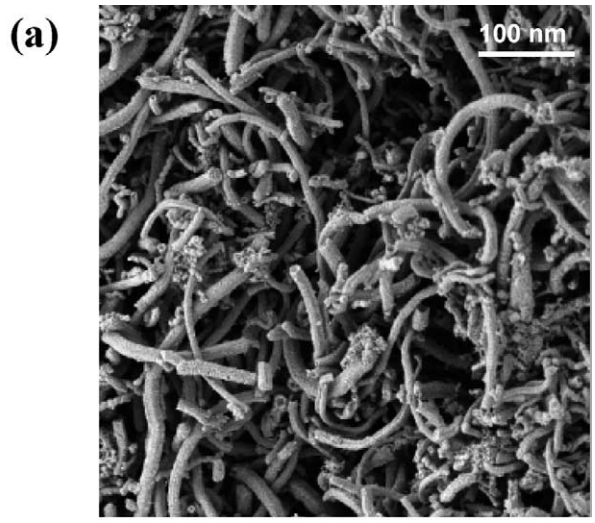


Fig. 3. Low (a) and higher (b) resolution SEM images showing structural features of carbon fibers grown from $Ni/SiO_2$: $T = 773$ K; $C_2H_4/H_2 = 4/1$ v/v.

product stream at higher reaction temperatures (> 873 K). The possibility of methane generation through a hydrogasification of the solid carbon product can be dismissed in this study as no methane was generated upon replacing ethylene with helium in mid-reaction; reintroduction of ethylene was accompanied by the reappearance of methane in the product stream. It is reasonable to conclude that methane is the result of a direct transformation of ethylene rather than from a subsequent carbon hydrogasification. At temperatures in excess of 873 K gasification of the activated carbon substrate did become a decided factor, limiting the usefulness of this support. The carbon yields delivered by each Ni catalyst at a fixed inlet $C_2H_4/H_2$ feed composition (4/1 v/v) are plotted in Fig. 4 as a function of reaction temperature. A wide range of yields (varying by over two orders of magnitude) is associated with these supported Ni systems with

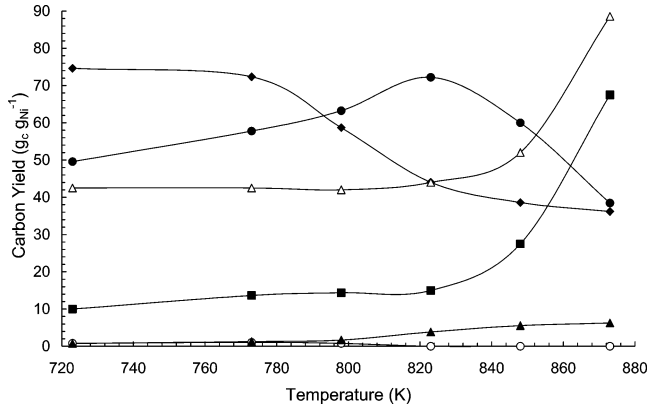


Fig. 4. Carbon yield (per gram of Ni) from (◆) $Ni/SiO_2$, (○) $Ni/Al_2O_3$, (▲) Ni/MgO, (■) Ni/AC, (△) Ni/graphite, and (●) $Ni/Ta_2O_5$ as a function of reaction temperature; $C_2H_4/H_2 = 4/1$ v/v, $t = 60$ min.

Table 2
Effect of $H_2$ content on the product selectivity at 773 K

| | Carbon | | | | Ethane | | | |
|---|---|---|---|---|---|---|---|---|
| % v/v $H_2$ in feed | 0 | 20 | 50 | 80 | 0 | 20 | 50 | 80 |
| (a) Selectivity after 5 min on stream (%) | | | | | | | | |
| $Ni/SiO_2$ | 54 | 96 | 56 | 56 | 46 | 4 | 44 | 44 |
| $Ni/Al_2O_3$ | 14 | 20 | 15 | 14 | 86 | 80 | 85 | 85 |
| Ni/AC | 70 | 79 | 54 | 54 | 30 | 21 | 46 | 46 |
| Ni/graphite | 89 | 69 | 76 | 67 | 11 | 31 | 24 | 33 |
| Ni/MgO | 13 | 18 | 14 | 18 | 87 | 82 | 86 | 82 |
| $Ni/Ta_2O_5$ | 93 | 77 | 71 | 58 | 7 | 23 | 29 | 42 |
| (b) Selectivity after 40 min on stream (%) | | | | | | | | |
| $Ni/SiO_2$ | 68 | 70 | 53 | 28 | 32 | 30 | 47 | 72 |
| $Ni/Al_2O_3$ | 13 | 18 | 15 | 11 | 87 | 81 | 85 | 89 |
| Ni/AC | 16 | 69 | 60 | 53 | 84 | 30 | 40 | 47 |
| Ni/graphite | 91 | 68 | 49 | 44 | 9 | 31 | 51 | 56 |
| Ni/MgO | 2 | 2 | 19 | 16 | 98 | 98 | 81 | 84 |
| $Ni/Ta_2O_5$ | 88 | 81 | 66 | 23 | 12 | 19 | 32 | 76 |

a diversity of temperature dependencies. The yields, for the most part, are comparable to those (20–70 $g_C/g_{metal}$) quoted elsewhere for supported Co, Fe, and Ni systems [39,65,66]. Carbon growth was least favored where Ni was supported on either an $Al_2O_3$ or MgO, regardless of the reaction temperature. Taking the product selectivities given in Table 2a and 2b, it is clear that ethylene hydrogenation to ethane is by far the preferred reaction over $Ni/Al_2O_3$ and Ni/MgO. Carbon growth from both Ni/AC and Ni/graphite was enhanced at higher temperatures (> 823 K) where the yield from Ni/graphite was consistently and appreciably greater. The carbon yield associated with $Ni/SiO_2$ declined at elevated temperatures and passed through an apparent maximum at 823 K over $Ni/Ta_2O_5$. Reaction temperature has been shown elsewhere to have a considerable bearing on the growth of ordered carbon [27,28,38,67]. Temperature-related carbon yield maxima have been reported [27,28,35,44] and the optimum temperature appears to be strongly dependent on the nature of both the catalyst and the feedstock. In this study, carbon yield (where $T < 800$ K) increased in the sequence $Ni/Al_2O_3 \sim$ Ni/MgO < Ni/AC < Ni/graphite < $Ni/Ta_2O_5$

$< Ni/SiO_2$; at higher temperatures ($> 850$ K), Ni dispersed on both carbonaceous substrates delivered the highest yields.

In the production of solid carbon, ethylene must first undergo a destructive chemisorption to generate carbon atoms that diffuse through the metal particle with subsequent precipitation. It is now generally accepted [68,69] that when the supported metal presents different exposed crystallographic planes to incoming reactant, significantly different catalytic reactivities can result. There can be a deal of specificity in the chemisorption step where certain Ni crystallographic orientations favor reactant decomposition [70,71]. The loss of hydrogen atoms with concomitant C–C bond scission is known to be facilitated by a thermodynamically driven multiple bonding of the chemisorbed hydrocarbon with the metal surface that serves to lower the surface free energy [72]. Ethylidyne, ethylidene, vinylidene, methylene, and methylidyne species have all been identified as species formed during the adsorption of ethylene on metal surfaces [72–74]. Cooper and Trimm have shown [75] that the rate of carbon deposition on an iron catalyst from a propylene feed is dependent on metal site geometry where Fe(100) > Fe(110). The predominant exposed metal face can be influenced by the choice of support and activation/pretreatment conditions [76,77]. In the case of $Ni/SiO_2$, the rate of ethane hydrogenolysis has been found [78–80] to correlate directly with the percentage of particles faces that adopted either a (100) or a (111) orientation; the Ni(111) face appears to favor carbon precipitation/growth [16,81]. The use of a graphitic carbon support has been shown to be a particularly effective means of altering the catalytic properties of supported metals [13,82,83], a response that has been accounted for in terms of electronic interactions between the metal and the $\pi$-electrons of graphite. While support-induced electronic effects are considered to be negligible for larger (ca. 10–40 nm) metallic particles [84], the distribution of Ni particle size associated with these catalysts (Fig. 2) is such that support effects can contribute, to varying degrees, to the metal site activity. The significant divergence of ethylene conversion and reaction selectivity (hydrogenation vs decomposition) observed in this study must result from differences in Ni particle morphology, exposed crystallographic orientations, and electronic character, all of which are influenced by the nature of the support.

### 3.3. Carbon growth: influence of hydrogen content

Hydrogen has been identified as a critical component in the catalytic growth of carbon nanofibers and is proposed to initiate hydrocarbon decomposition [20,27–37,42,50,51] while also influencing the graphitic nature of the carbon product [85,86]. However, Herreyre and Gadelle [87] have found that $H_2$ is not essential for carbon production and this is borne out in Tables 2 and 3. Even with a prolonged flushing of the reduced catalysts in He, the yield of carbon from a $C_2H_4$/He feed was appreciable over Ni/AC, Ni/graphite, and $Ni/Ta_2O_5$. It should be noted that a destructive chemisorption of ethylene on the surface Ni results in a concomitant production of C and $H_2$. Moreover, flushing with He need not remove all residual surface hydrogen, which can contribute to the decomposition step, and with the associated $H_2$ evolution, the reaction is, in a sense, self-sustaining. With the exception of the less active $Ni/Al_2O_3$ and Ni/MgO, carbon yield was, nevertheless, sensitive to the $H_2$ content where $Ni/SiO_2$ delivered enhanced carbon growth at higher $H_2$ feedstock content (Table 3). The response of reaction selectivity to changes in hydrogen feed content can be assessed from the entries in Tables 2a and 2b, wherein carbon selectivity typically declined with time on stream. The overall consumption of ethylene was largely time invariant after the first 10 min and the selectivities quoted in Table 2b were recorded at steady-state activities. The carbon yields given in Table 3 refer to a 60-min reaction period which can be taken to be representative of the growth process and a suitable point of comparison for each catalyst. A depletion in carbon growth with extended reaction time has been noted elsewhere and attributed to an encapsulation of those sites active in hydrocarbon decomposition by a carbon overlayer [30,31]. As was the case with temperature variations, Ni/MgO or $Ni/Al_2O_3$ exhibited little in the way of a selectivity dependence on hydrogen content and ethane formation predominated. Reaction selectivity associated with $Ni/SiO_2$ was certainly sensitive to $H_2$ content with an apparent selectivity maximum at 20% v/v $H_2$. Carbon deposition selectivity delivered by Ni/graphite (and $Ni/Ta_2O_5$ to a lesser extent) at 773 K exhibited a decline at higher inlet $H_2/C_2H_4$ feed ratios. It is significant that carbon growth from the two catalysts that exhibit SMSI behavior is most susceptible to changes in the reactant feed. The increase in the hydrogen content may have resulted in a reconstruction of the metal particles where carbon production was less favored. The latter should also impact on the carbon structural features, an effect that is probed below.

Table 3
Carbon yield, after 1 h on stream, as a function of hydrogen content at two reaction temperatures

| | Carbon yield ($g_C/g_{cat}$) at 773 K | | | | Carbon yield ($g_C/g_{cat}$) at 823 K | | | |
|---|---|---|---|---|---|---|---|---|
| % v/v $H_2$ in feed | 0 | 20 | 50 | 80 | 0 | 20 | 50 | 80 |
| $Ni/SiO_2$ | 1.6 | 1.9 | 2.0 | 7.2 | 0.7 | 2.0 | 2.2 | 4.4 |
| $Ni/Al_2O_3$ | < 0.1 | < 0.1 | < 0.1 | 0.1 | 0.3 | 0.3 | 0.1 | < 0.1 |
| Ni/AC | 6.1 | 1.2 | 2.1 | 1.1 | 3.3 | 3.3 | 3.7 | 1.2 |
| Ni/graphite | 4.6 | 3.1 | 7.4 | 4.3 | 2.6 | 3.8 | 5.3 | 4.4 |
| Ni/MgO | 0.3 | 0.3 | 0.2 | 0.1 | 0.2 | 0.4 | < 0.1 | 0.3 |
| $Ni/Ta_2O_5$ | 3.9 | 3.8 | 5.8 | 5.2 | 3.4 | 4.1 | 5.2 | 6.5 |

### 3.4. Carbon growth: structural features

Temperature-programmed oxidation was employed to evaluate the extent of carbon structural order, i.e., amorphous and/or graphitic nature. It is well established that an increasing order in the carbon structure is accompanied by an elevation of the temperature at which gasification is in-

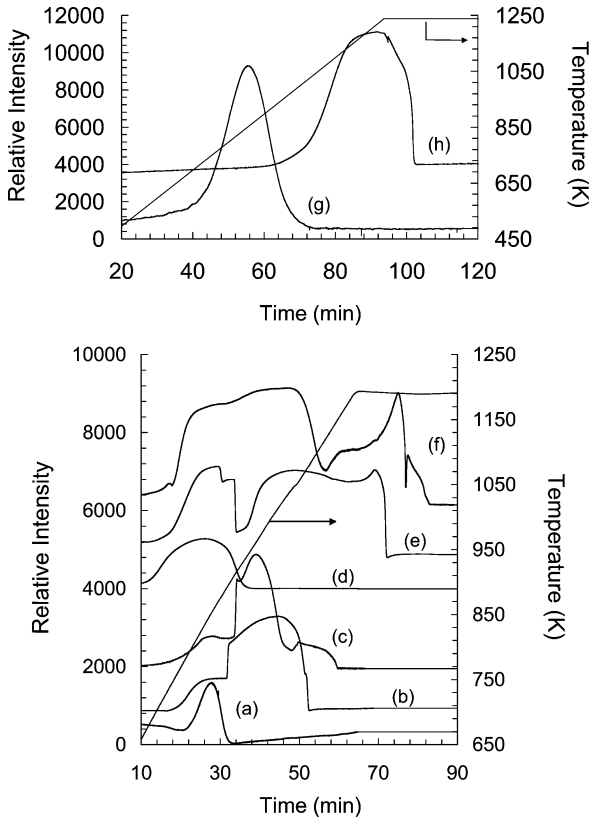


Fig. 5. TPO profiles of demineralized carbon nanofiber samples generated from (a) Ni/MgO ($T_{max} = 850$ K), (b) Ni/$Ta_2O_5$ ($T_{max} = 1100$ K), (c) Ni/$SiO_2$ ($T_{max} = 970$ K), (d) Ni/$Al_2O_3$ ($T_{max} = 840$ K), (e) Ni/AC ($T_{max} = 850$, 1030, 1200 K), and (f) Ni/graphite ($T_{max} = 855$, 1035, 1200 K): $C_2H_4/H_2 = 4/1$ v/v; $T = 773$ K. Inset: TPO profiles of model demineralized carbons: (g) activated carbon ($T_{max} = 821$ K); (h) graphite ($T_{max} = 1130$ K); relative intensity has arbitrary units.

duced [88]. The TPO profiles of carbon grown from the six supported Ni catalysts (under the same reaction conditions) can be compared in Fig. 5 and assessed against the profiles associated with model-activated carbon and graphite; the principal characteristic TPO $T_{max}$ values are included in the Fig. 5 legend. It is immediately apparent that the catalytically generated carbon exhibits an appreciable structural diversity. Carbon grown from Ni/$Al_2O_3$ and Ni/MgO is essentially amorphous in nature with evidence of limited overall structural order. The Ni/$SiO_2$ and Ni/$Ta_2O_5$ catalysts delivered a more graphitic product on the basis of the shift in oxidation profile to a higher temperature regime, but there is still a significant amorphous component. TPO analysis of the carbon generated from Ni/AC and Ni/graphite is problematic in that the TPO response of the catalytically grown carbon is masked to some extent by the oxidation of the substrate. Nevertheless, it is evident that Ni/graphite and Ni/AC delivered a range of carbonaceous products, judging from the broad oxidation profiles. By comparison with TPO profiles Fig. 5g and h, Ni/AC produced a carbon product that is significantly more graphitic than the substrate while the spent Ni/graphite possessed both an amorphous and a structured component, the latter characterized by a higher

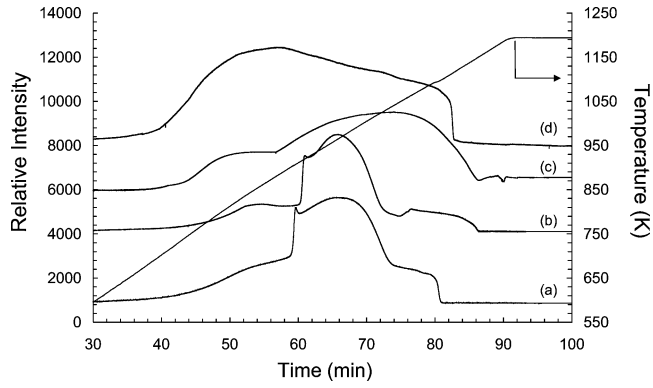


Fig. 6. TPO profiles of the demineralized samples of carbon nanofibers generated from Ni/$SiO_2$ at different reaction temperatures: (a) $T = 773$ K ($T_{max} = 970$ K); (b) $T = 823$ K ($T_{max} = 985$ K); (c) $T = 873$ K ($T_{max} = 810$, 1050 K); (d) $T = 898$ K ($T_{max} = 875$, 1090 K); $C_2H_4/H_2 = 4/1$ v/v; relative intensity has arbitrary units.

Table 4
Effect of the $H_2$ feed content on the $T_{max}$ of the TPO profiles associated with carbon fiber growth from Ni/$SiO_2$ and Ni/$Ta_2O_5$: $T = 773$ K; $t = 60$ min

| % v/v $H_2$ in feed | $T_{max}$ (K) | |
|---|---|---|
| | Ni/$SiO_2$ | Ni/$Ta_2O_5$ |
| 0 | 920 | 1020 |
| 20 | 970 | 1100 |
| 50 | 1045 | 1110 |
| 80 | 1090 | 1130 |

$T_{max}$ than that recorded for model graphite (see legend of Fig. 5). These observations point to a strong contribution of the support in determining the structural characteristics of the carbon product. The degree of structural order was also dependent on reaction temperature, as illustrated in Fig. 6 where the carbon generated from Ni/$SiO_2$ shows greater graphitic character on raising the reaction temperature from 773 to 873 K. Where $T > 873$ K, there was some evidence of additional amorphous growth, characterized by a broad low temperature peak, which is presumably the result of a thermal (noncatalytic/nonselective) decomposition of ethylene [89]. Reaction temperatures in excess of 873 K have been noted elsewhere to have a deleterious effect on carbon grown from bimetallic catalysts [27]. The effect of the $H_2$ content in the reactant feed on the TPO characteristics is revealed in Table 4 for carbon growth from Ni/$SiO_2$ and Ni/$Ta_2O_5$. In both cases, carbon structural order was enhanced by increasing the $H_2/C_2H_4$ inlet ratio. Taking an overview of all the TEM analyses that have been conducted, it is fair to state that the integrity of the fiber graphitic structure in terms of lattice uniformity increased with increasing $H_2$ feed content. Moreover, a greater faceting of the Ni component was evident for the higher $H_2$ content feed, a phenomenon that has been reported elsewhere [27,28]. There is growing consensus in the literature [22] that carbon precipitated from the faceted particles is significantly more ordered.

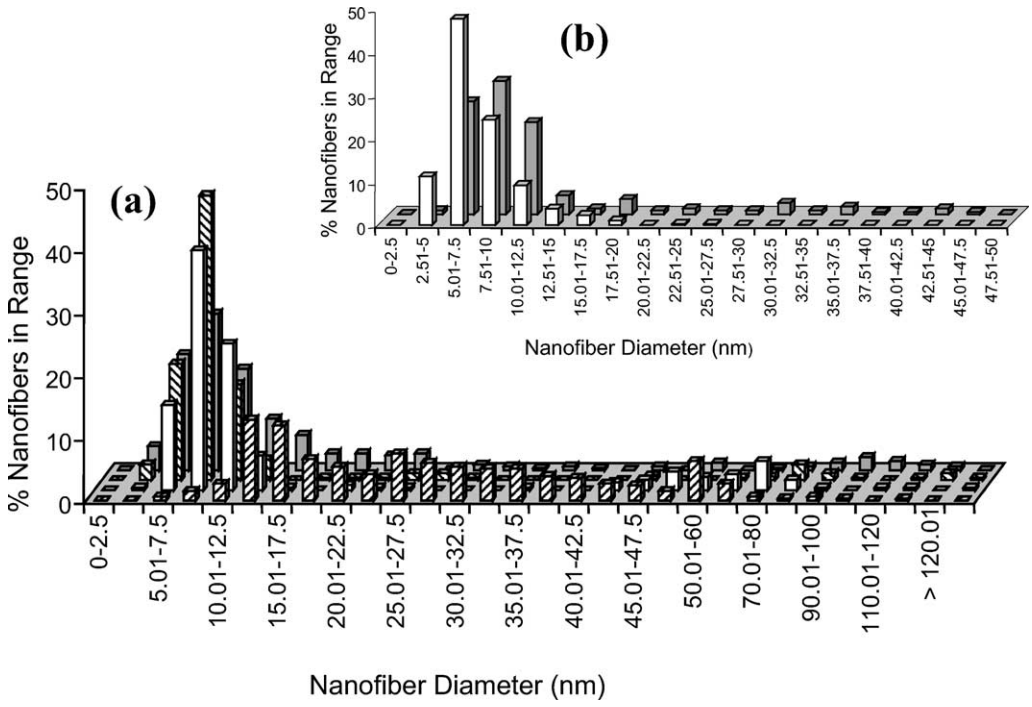


Fig. 7. (a) Carbon nanofiber diameter distributions associated with Ni/AC (solid bars), Ni/graphite (downward hatched bars), $Ni/Ta_2O_5$ (open bars), and $Ni/SiO_2$ (upward hatched bars). (b) Inset, $Ni/Al_2O_3$ (solid bars) and Ni/MgO (open bars): $C_2H_4/H_2 = 4/1$; $T = 773$ K, $t = 60$ min.

Table 5
Average nanofiber diameters (with size distribution) associated with each Ni-supported catalyst: $T = 773$ K; $t = 60$ min; $C_2H_4/H_2 = 4/1$ v/v

| Catalyst | Average carbon nanofiber diameter (nm) | % Nanofibers | |
|---|---|---|---|
| | | $d \leqslant 15$ nm | $d \leqslant 25$ nm |
| $Ni/SiO_2$ | 25.4 | 18 | 46 |
| $Ni/Al_2O_3$ | 13.4 | 84 | 90 |
| Ni/AC | 19.7 | 71 | 85 |
| Ni/graphite | 17.0 | 83 | 84 |
| Ni/MgO | 8.7 | 96 | > 99 |
| $Ni/Ta_2O_5$ | 23.3 | 81 | 83 |

The broadness and diversity of the TPO peaks are also indicative of a range of nanofiber diameters where fiber diameter/availability of edge sites can impact on gasification characteristics. The surface-weighted average nanofiber diameters derived from TEM analyses are given in Table 5, wherein it is evident that there is a significant range of fiber diameters/size distributions. By far the narrowest fibers were grown from Ni/MgO, although the yield was very low (Table 3). The least control, in terms of fiber dimension, was imposed by $Ni/SiO_2$. The dimensions of the seed Ni particle should determine the ultimate width of the fiber. The carbon fiber diameter distribution is illustrated by the histograms given in Fig. 7. The first noticeable feature is that apart from Ni/MgO, an ineffective carbon growth catalyst, the nanofibers exhibited bimodal size distributions. The carbon associated with $Ni/SiO_2$ is characterized by a very broad distribution with appreciable tailing. A comparison of the fiber diameter distribution (Fig. 7) with the Ni particle-size distribution in the freshly activated catalysts (Fig. 2) suggests some Ni particle growth/sintering during reaction. Anderson and Rodriguez [31] observed that $SiO_2$-supported Fe:Ni bimetallics readily underwent sintering and possible reconstruction to generate carbon nanofibers (from a $CO/H_2$ feed) with diameters typically twice that of the freshly reduced metal crystallites. Of direct relevance to this study, Takenaka et al. [90] have reported an induced aggregation of Ni particles on $SiO_2$ during methane decomposition at 803 K. There is no direct or obvious match of initial metal diameter with final fiber width. A TEM analysis of Ni/MgO and $Ni/Al_2O_3$ after reaction revealed that a significant component of the surface Ni did not have any associated carbon growth. The observed nanofiber distribution can then be considered to reflect the size of Ni particles of the requisite orientation allied to particle growth during reaction. Bimodal distribution aside, and focusing on appreciable carbon growth, $Ni/Ta_2O_5$ and Ni/graphite provide the greatest carbon yield under 15 nm in diameter, in keeping with the stronger Ni/substrate interactions that limit Ni sintering and, as a direct consequence, fiber diameter.

The effect(s) of varying the Ni support on the structural characteristics of the carbon fibers can be assessed from the TEM images presented in Figs. 8–13, wherein fibers of varying diameter and morphology are in evidence. The carbon grown from $Ni/SiO_2$ (Fig. 8a) can be characterized as relatively straight nanofibers, many possessing an ill-defined hollow central core. The two predominant lattice arrangements associated with the fibers produced in this study are shown in Fig. 9: the so-called "ribbon" form [16,27] where the carbon platelets are oriented in an arrangement that is parallel to the fiber axis (Fig. 9a), and the "fishbone" con-

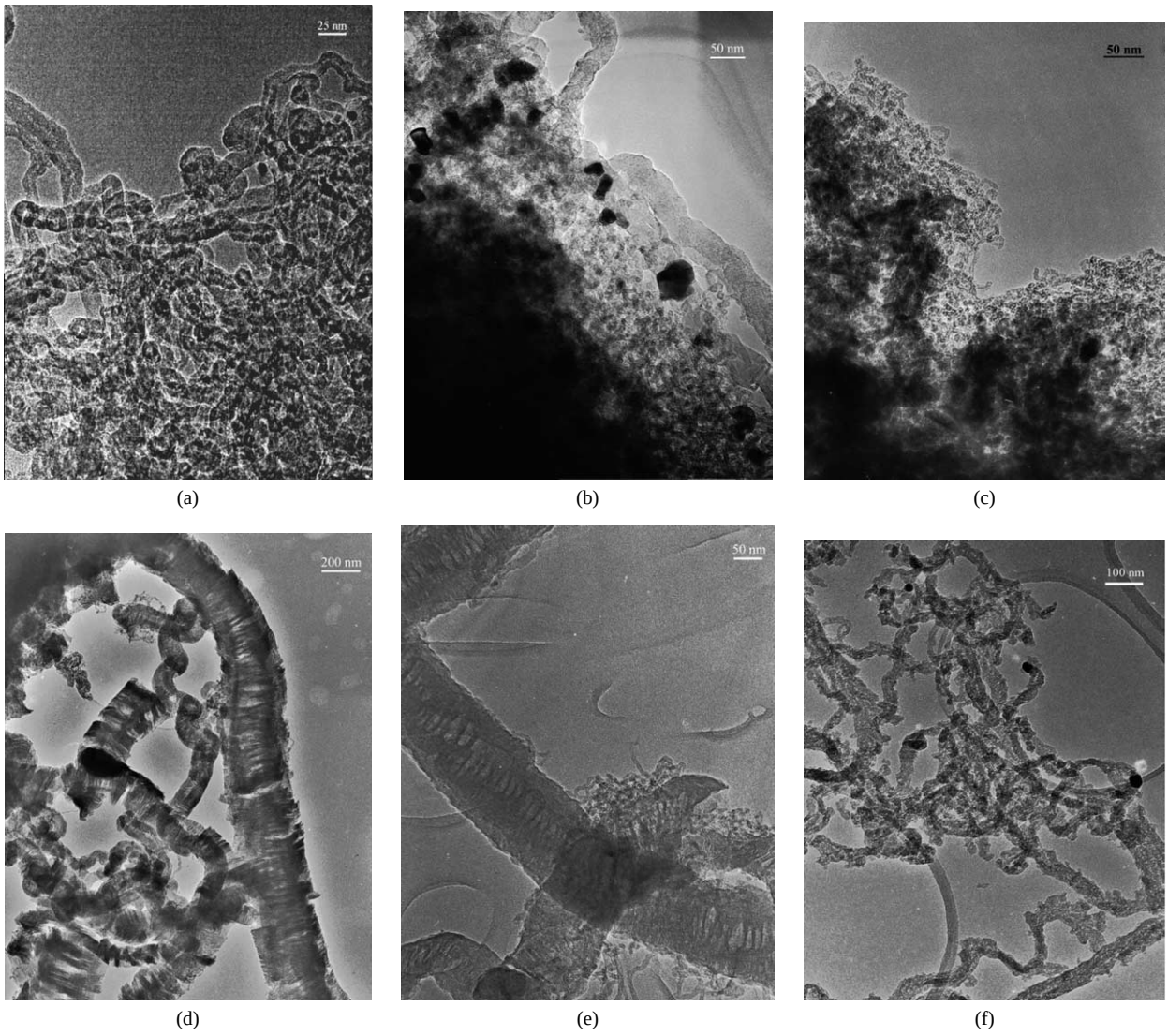


Fig. 8. Low-magnification TEM images showing the nature and extent of carbon growth from (a) $Ni/SiO_2$, (b) $Ni/Al_2O_3$, (c) Ni/MgO, (d) $Ni/Ta_2O_5$, (e) Ni/graphite, and (f) Ni/AC: $T = 773$ K; $C_2H_4/H_2 = 4/1$ v/v; $t = 60$ min.

figuration where the platelets are parallel and oriented at an angle to the fiber axis [16,38]. The interplatelet spacing of ca. 0.34 nm is diagnostic of a graphitic species. It must be stressed that all the images presented here are of carbon samples taken directly from the catalytic reactor without any purification. The presence of an amorphous carbon layer visible on the fiber edges is an artifact of the cooling stage, upon completion of the catalytic step. The limited structural carbon associated with $Ni/Al_2O_3$ (Fig. 8b) and Ni/MgO (Fig. 8c) exhibited essentially the same morphology as that produced by $Ni/SiO_2$ but the interlayer spacings were not uniform and there was a preponderance of structural defects and partial layers; the narrower fibrous growth associated with Ni/MgO is discernible in Fig. 8c.

In marked contrast, carbon grown from $Ni/Ta_2O_5$ (Fig. 8d) and Ni/graphite (Fig. 8e) is helical in nature, exhibiting a greater degree of curvature than was observed for the other catalysts. The growth of spiral (or helical) carbon fibers can be attributed to an unequal diffusion of carbon through the metal particle, leading to an anisotropic growth. Such growth, as opposed to straighter fiber production can again be linked to different exposed Ni orientations on the substrates considered in this work. Zaikovskii and coworkers [91], using an MgO-supported bimetallic Ni–Cu catalyst, generated symmetrical spiral nanofibers. These authors proposed that a carbide mechanism was in operation where metastable $Ni_3C$ exists during the hydrocarbon transformation before decomposing to metal and carbon. It was suggested that the different diffusional pathways taken by the carbon atoms through the carbide phase lead to different rates of carbon growth, resulting in a "twisted" or spiral growth. The manner in which the morphology of the Ni particle can influence the shape and orientation of the carbon growth is illustrated in Fig. 10 for $Ni/Ta_2O_5$. A reconstruction of the seed metal particle during carbon growth has been noted elsewhere [92,93]. The Ni particle exhibited a

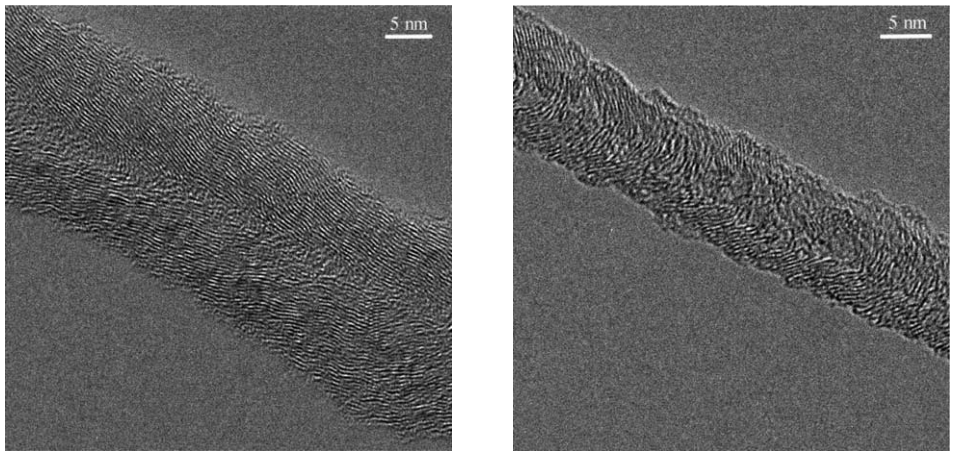


Fig. 9. High-resolution TEM images of isolated carbon fibers grown from $Ni/SiO_2$ that exhibit platelets arrayed (a) parallel to and (b) at an angle to the fiber axis: $T = 773$ K; $C_2H_4/H_2 = 4/1$ v/v.

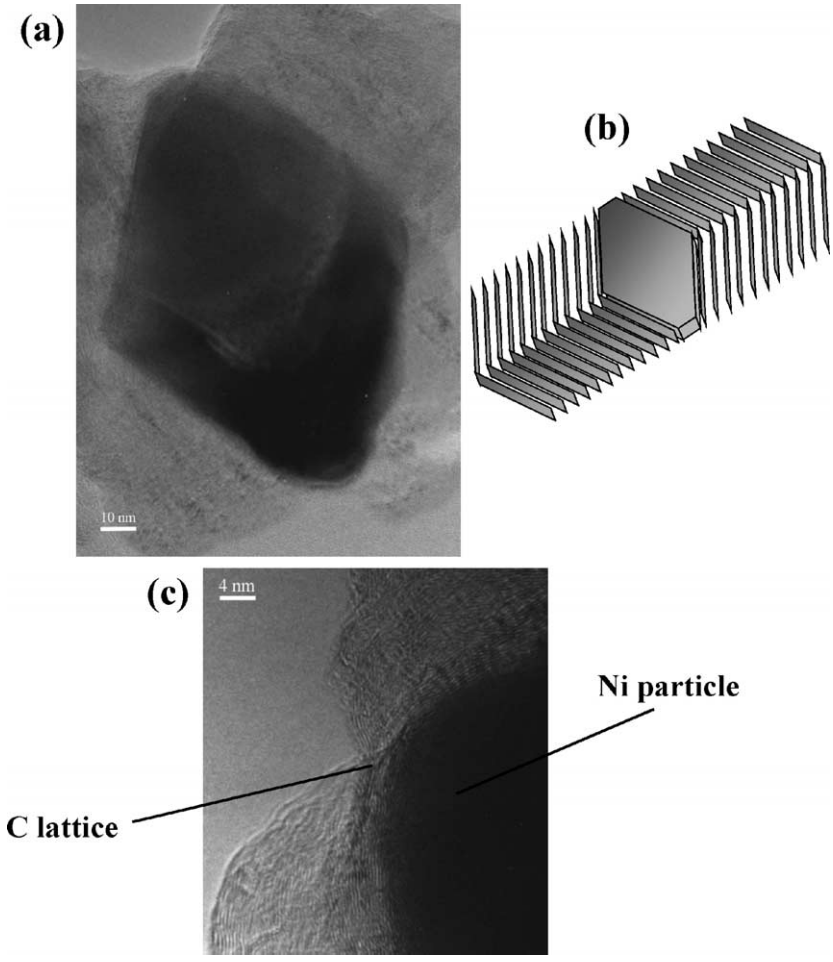


Fig. 10. High-resolution TEM images of carbon grown from $Ni/Ta_2O_5$ showing (a) an entrapped rhombohedrical Ni particle with (b) simple schematic representation and (c) Ni particle edge/carbon lattice structure: $C_2H_4/H_2 = 4/1$ v/v; $T = 773$ K; $t = 60$ min.

predominant pill-box shape after reduction (Fig. 1e) but underwent reconstruction to a rhombohedral-shaped particle (Fig. 10a) in the presence of the reactant gas. The simple schematic included in Fig. 10b illustrates the link between the Ni site and the ultimate nanofiber growth. It can be seen (Fig. 10c) that the carbon layers adopt geometries that complement that associated with the edge of the reconstructed Ni particle. Carbon diffusion through these particles generates

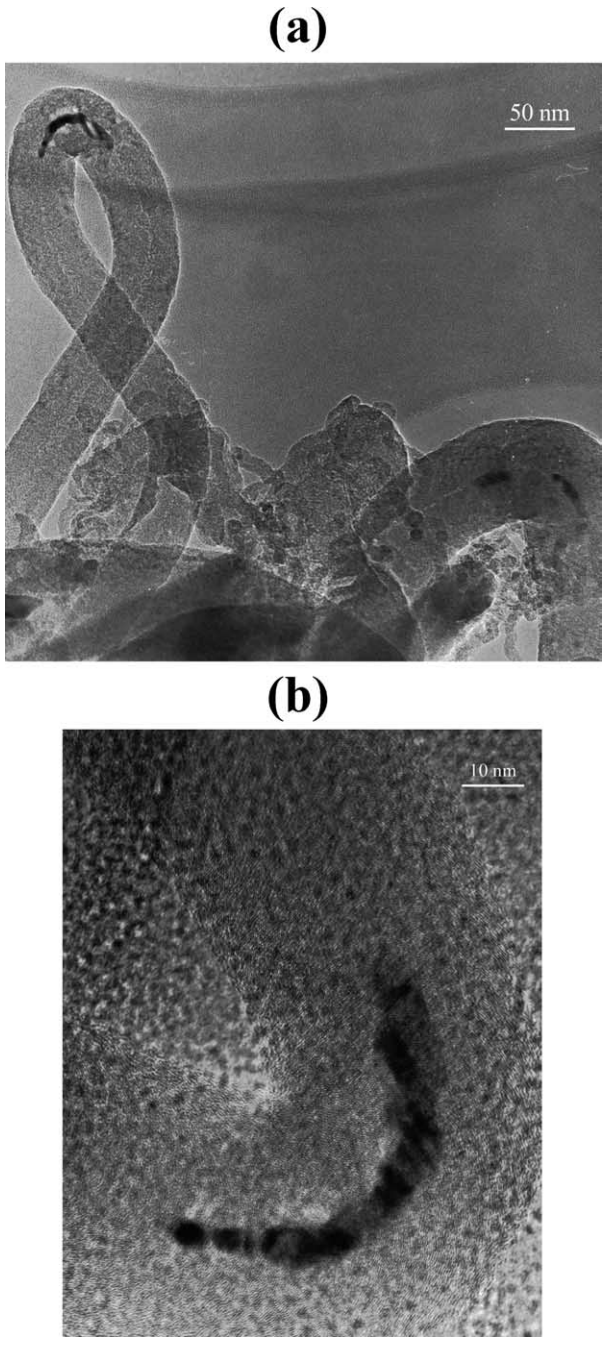


Fig. 11. Low- (a) and high- (b) magnification TEM images of carbon nanofibers grown from $Ni/Ta_2O_5$ ($C_2H_4/H_2 = 4/1$ v/v, $T = 773$ K), showing Ni fragment inclusion.

an unequal deposition at the rear face which manifests itself in the form of a spiral/coiled fiber. The carbon generated in this instance is more ordered in that from (say) $Ni/Al_2O_3$ but it still possesses many defects and is not as structured as that of graphite, which is in keeping with the TPO analysis. One feature common to carbon growth observed in this study is the occurrence of Ni inclusions in the growing fiber; this effect is shown in Fig. 11, taking $Ni/Ta_2O_5$ as a representative catalyst. The movement of carbon atoms through the Ni lattice necessitates a displacement of Ni atoms [94] where the pressure exerted on the Ni/support interface due to graphite formation must be of sufficient magnitude to extract Ni particles from the substrate. A magnified view of the nature of a metal inclusion and the orientation of the local graphite platelets is given in Fig. 11b. The metal inclusions are not trivial (lengths up to 70 nm, diameters $< 10$ nm), equating to a sizeable component of the starting metal content. Whether the metal is included within the confines of the hollow channel that runs along the length of the nanofiber or whether it is situated on the outer nanofiber surface has yet to be conclusively established. As there was no evidence of any secondary fibers generated from these metal inclusions under conditions of prolific carbon growth, it seems more likely that the metal is situated within the nanofiber rather than a surface artifact.

Carbon generated from Ni/AC is characterized by a "rough" exterior (Fig. 8f). Under higher magnification (Fig. 12), a secondary growth of smaller fibers is visible associated with the main fiber. This growth of smaller nanofibers ($d < 20$ nm) from larger fibers ($d > 60$ nm) is the source of the bimodal size distribution shown in Fig. 7. The latter effect suggests that the Ni particle associated with the original fiber growth fragmented, resulting in the deposition of small Ni particles on the main fiber that remained accessible to incoming $C_2H_4$ and participated in the growth process to produce (secondary) smaller diameter nanofibers. The weaker metal/support interactions that characterize Ni/AC can facilitate Ni metal fragmentation/extraction. Reconstruction of the Ni particles supported on the graphite substrate was also a feature of the carbon growth process as is illustrated by the TEM image given in Fig. 13 wherein the helical carbon growth is in evidence. The appreciable Ni site reconstruction can be assessed from comparison with the metal morphology that characterizes the freshly activated sample (Fig. 1a). Indeed, the occurrence of a central hollow core in the fibers (see Figs. 8 and 9) can also be attributed to a deformation or faceting of the supported metal particle that alters the relative rate of carbon diffusion and fiber nucleation.

## 4. Conclusions

Impregnation and activation of Ni on various oxide and carbon based substrates have led to significant variations in the intrinsic catalytic activity/selectivity of the supported Ni for the reaction of ethylene with hydrogen to generate ethane (hydrogenation) and/or carbon (decomposition). The carbon product takes the form of nanofibers of varying structural integrity and an amorphous carbon component. Carbon deposition was favored over Ni/AC, Ni/graphite, $Ni/Ta_2O_5$, and $Ni/SiO_2$ while ethylene hydrogenation predominated over $Ni/Al_2O_3$ and Ni/MgO. Variations in reaction selectivity can be ascribed to differences in metal/support interaction(s) where, in the case of Ni dispersed on $Al_2O_3$ and MgO, the metal is in a predominant crystallographic ori-


Fig. 12. TEM images demonstrating the nature/morphology of the carbon growth from Ni/AC: $T = 773$ K; $C_2H_4/H_2 = 4/1$ v/v; $t = 60$ min.

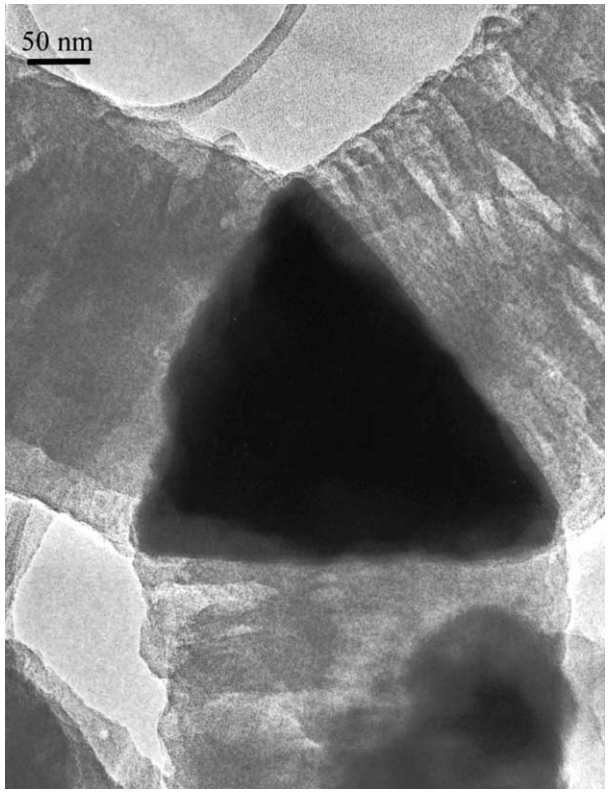


Fig. 13. TEM image showing structural features associated with carbon grown from Ni/graphite: $C_2H_4/H_2 = 4/1$; $T = 773$ K; $t = 60$ min.

entation that did not favor a destructive chemisorption of ethylene but rather facilitated hydrogenation to ethane. The six catalyst systems exhibit a diversity of temperature dependencies in terms of carbon yield and fiber morphology. At temperatures in excess of 850 K, Ni/graphite and Ni/AC generated the highest yields but at lower temperatures $Ni/SiO_2$ and $Ni/Ta_2O_5$ delivered the more effective carbon growth. The fibrous product, in the main, showed little curvature with the exception of Ni/graphite and $Ni/Ta_2O_5$, which produced highly curved/helical structures. The $H_2$ content in the feed is a critical reaction variable where a higher content facilitated a more ordered growth. Nickel fragmentation is typical in these systems where the Ni metal fragments can be dispersed on the growing carbon and serve to promote a secondary (narrower) growth from the original carbon fiber, an effect that is particularly prevalent in the case of Ni/AC.

## Acknowledgment

The authors thank Dr. R. Brydson for access to TEM facilities.

## References

[1] I.J. Adadurov, J. Phys. Chem. USSR 6 (1935) 206.
[2] G.L. Haller, D.E. Resasco, Adv. Catal. 132 (1991) 269.
[3] G.M. Schwab, Adv. Catal. 27 (1982) 1.
[4] V. Ponec, Stud. Surf. Sci. Catal. 11 (1982) 63.

[5] X.-Z. Jiang, S.A. Stevenson, J.A. Dumesic, J. Catal. 91 (1985) 11.
[6] A.Y. Stakheev, L.M. Kustov, Appl. Catal. A 188 (1999) 3.
[7] B.C. Gates, Chem. Rev. 95 (1995) 511.
[8] S.J. Tauster, S.C. Fung, R.L. Garten, J. Am. Chem. Soc. 100 (1978) 170.
[9] M.A. Vannice, J. Catal. 74 (1982) 199.
[10] L.M. Tau, C.O. Bennett, J. Catal. 89 (1984) 285.
[11] C.H. Bartholomew, R.B. Pannell, J.L. Butler, J. Catal. 65 (1980) 335.
[12] S.J. Tauster, S.C. Fung, R.T.K. Baker, J.A. Horsley, Science 211 (1981) 1121.
[13] F. Salman, C. Park, R.T.K. Baker, Catal. Today 53 (1999) 385.
[14] R.T.K. Baker, E.B. Prestridge, R.L. Garten, J. Catal. 56 (1979) 390.
[15] M.S. Hoogenraad, R.A.G.M.M. van Leeuwarden, G.J.B. van Breda Vriesman, A. Broersma, A.J. van Dillen, J.W. Geus, Stud. Surf. Sci. Catal. 101 (1996) 263.
[16] K.P. de Jong, J.W. Geus, Catal. Rev.-Sci. Eng. 42 (2000) 481.
[17] C. Menini, C. Park, R. Brydson, M.A. Keane, J. Phys. Chem. B 104 (2000) 4281.
[18] C.N.R. Rao, B.C. Satishkumar, A. Govindaraj, M. Nath, Chem. Phys. Chem. 2 (2001) 78.
[19] M.S. Dresselhaus, Science 292 (2001) 650.
[20] R.T.K. Baker, Carbon 27 (1989) 315.
[21] R.T.K. Baker, K. Laubernds, A. Wootsch, Z. Paál, J. Catal. 193 (2000) 165.
[22] C. Park, R.T.K. Baker, J. Phys. Chem. B 102 (1998) 5168.
[23] C. Pham-Huu, N. Keller, L.J. Charbonniere, R. Ziessle, M.J. Ledoux, Chem. Commun. (2000) 1871.
[24] K. Lozano, E.V. Barrera, J. Appl. Polm. Sci. 79 (2001) 125.
[25] C.A. Bessel, K. Laubernds, N.M. Rodriguez, R.T.K. Baker, J. Phys. Chem. B 115 (2001) 1115.
[26] C. Park, E.S. Engel, A. Crowe, T.R. Gilbert, N.M. Rodriguez, Langmuir 16 (2000) 8050.
[27] C. Park, N.M. Rodriguez, R.T.K. Baker, J. Catal. 169 (1997) 212.
[28] C. Park, R.T.K. Baker, J. Catal. 179 (1998) 361.
[29] R.T.K. Baker, M.S. Kim, A. Chambers, C. Park, N.M. Rodriguez, in: C.H. Bartholomew, G.A. Fuentes (Eds.), Catalyst Deactivation, Elsevier, Amsterdam, 1997, p. 99.
[30] C. Park, M.A. Keane, Langmuir 17 (2001) 8386.
[31] P.E. Anderson, N.M. Rodriguez, Chem. Mater. 12 (2000) 823.
[32] I. Willems, Z. Kónya, J.-F. Colomer, G. van Tendeloo, N. Nagaraju, A. Fonseca, J.B. Nagy, Chem. Phys. Lett. 317 (2000) 71.
[33] K. Hernadi, A. Fonseca, J.B. Nagy, A. Siska, I. Kiricsi, Appl. Catal. A 199 (2000) 245.
[34] P. Piedigrosso, Z. Kónya, J.-F. Colomer, A. Fonseca, G. van Tendeloo, J.B. Nagy, Phys. Chem. Chem. Phys. 2 (2000) 163.
[35] J.-F. Colomer, C. Stephan, S. Lefrant, G. van Tendeloo, I. Willems, Z. Konya, A. Fonseca, Ch. Laurent, J.B. Nagy, Chem. Phys. Lett. 317 (2000) 83.
[36] L.B. Avdeeva, D.I. Kochubey, S.K. Shaikhutdinov, Appl. Catal. A 177 (1999) 43.
[37] L.B. Avdeeva, O.V. Goncharova, D.I. Kochubey, V.I. Zaikovskii, L.M. Plyasova, B.N. Novgorodov, S.K. Shaikhutdinov, Appl. Catal. A 141 (1996) 117.
[38] N.M. Rodriguez, J. Mater. Res. 8 (1993) 3233.
[39] P.E. Anderson, N.M. Rodriguez, J. Mater. Res. 14 (1999) 2912.
[40] S.J. Tauster, S.C. Fung, J. Catal. 55 (1978) 29.
[41] K. Sakanishi, H. Hasuo, I. Mochida, O. Okuma, Energy Fuels 9 (1995) 995.
[42] R.T.K. Baker, J. Catal. 63 (1980) 523.
[43] R.T.K. Baker, E.B. Prestridge, G.B. McVicker, J. Catal. 89 (1984) 422.
[44] Y. Ding, G. Zhang, H. Wu, B. Hai, L. Wang, Y. Qian, Chem. Mater. 13 (2001) 435.
[45] Y.D. Li, M. Sui, Y. Ding, G. Zhang, J. Zhuang, C. Wang, Adv. Mater. 12 (2000) 818.
[46] O.B. Koper, I. Lagadic, A. Volodin, K. Klabunde, J. Chem. Mater. 9 (1997) 2468.
[47] C. Hoang-Van, Y. Kachaya, S.J. Teichner, Appl. Catal. 46 (1989) 281.
[48] M.I. Zaki, Stud. Surf. Sci. Catal. 100 (1996) 569.
[49] C. Park, R.T.K. Baker, J. Phys. Chem. B 104 (2000) 4418.
[50] C. Park, M.A. Keane, Catal. Commun. 2 (2001) 171.
[51] C. Park, M.A. Keane, Solid State Ionics 141–142 (2001) 191.
[52] P. Burattin, M. Che, C. Louis, J. Phys. Chem. B 101 (1997) 7060.
[53] M.A. Keane, Can. J. Chem. 72 (1994) 372.
[54] E. Boellaard, A.M. van der Kraan, J.W. Geus, Appl. Catal. A 224 (2002) 1.
[55] J.S. Smith, P.A. Thrower, M.A. Vannice, J. Catal. 68 (1981) 270.
[56] J.W.E. Coenen, Appl. Catal. 75 (1991) 193.
[57] E. Garrone, A. Zecchina, F.S. Stone, J. Chem. Soc., Faraday Trans. 84 (1988) 2843.
[58] M.A. Babaeva, D.S. Bystrov, A.A. Tsygannenko, J. Catal. 123 (1990) 396.
[59] X. Lu, X. Xu, N. Wang, Q. Zhang, J. Phys. Chem. B 103 (1999) 3373.
[60] J. Adamiec, S.E. Wanke, B. Tesche, U. Klenger, Stud. Surf. Sci. Catal. 11 (1982) 77.
[61] N. Vasquez, A. Muscat, R.J. Madix, Surf. Sci. 310 (1994) 83.
[62] J.L. Falconer, J.A. Schwartz, Catal. Rev.-Sci. Eng. 25 (1983) 141.
[63] F. Arena, F. Frusteri, A. Parmaliana, Appl. Catal. A 187 (1997) 127.
[64] R.T.K. Baker, P.S. Harris, in: P.L. Walker Jr., P.A. Thrower (Eds.), Chemistry and Physics of Carbon, Dekker, New York, 1978, p. 83.
[65] R. van Hardeveld, F. Hartog, Adv. Catal. 18 (1972) 75.
[66] M.A. Ermakova, D.Yu. Ermalov, A.L. Chuvilin, G.G. Kuvshinov, J. Catal. 201 (2001) 183.
[67] K. Hernadi, A. Fonseca, J.B. Nagy, D. Bernaerts, A. Fudala, A.A. Lucas, Zeolites 17 (1996) 416.
[68] D.R. Rainer, D.W. Goodman, J. Mol. Catal. A: Chem. 131 (1998) 259.
[69] D.R. Rainer, X.P. Xu, D.W. Goodman, J. Mol. Catal. A: Chem. 119 (1997) 307.
[70] I. Alstrup, J. Catal. 109 (1988) 241.
[71] T.E. Müller, D.G. Reid, W.K. Hsu, J.P. Hare, H.W. Kroto, D.R.M. Walton, Carbon 35 (1997) 951.
[72] G.C. Bond, Appl. Catal. A 149 (1997) 3.
[73] S.M. Davis, F. Zaera, G.A. Somorjai, J. Catal. 77 (1982) 439.
[74] V. Ponec, G.C. Bond, Catalysis by Metals and Alloys, Elsevier, Amsterdam, 1995.
[75] B.J. Cooper, D.L. Trimm, J. Catal. 62 (1980) 35.
[76] Y. Aray, J. Rodriguez, J. Rivero, D. Vega, Surf. Sci. 441 (1999) 344.
[77] E.I. Ko, R.L. Garten, J. Catal. 68 (1981) 237.
[78] D.E. Resasco, G.L. Haller, in: B. Imelik, C. Naccache, G. Coudurier, H. Praliaud, P. Meriaudeau, P. Gallezot, G.A. Martin, J.C. Vedrine (Eds.), Metal–Support and Metal–Additive Effects in Catalysis, Elsevier, Amsterdam, 1982, p. 105.
[79] D.W. Goodman, Catal. Today 12 (1992) 189.
[80] K. Coulter, X.P. Xu, D.W. Goodman, J. Phys. Chem. 98 (1994) 1245.
[81] F. Frusteri, L. Spadaro, F. Arena, A. Chuvilin, Carbon 40 (2002) 1063.
[82] J. Ma, N.M. Rodriguez, M.A. Vannice, R.T.K. Baker, J. Catal. 183 (1999) 32.
[83] J.-H. Kim, D.J. Suh, T.-J. Park, K.-L. Kim, Appl. Catal. A 197 (2000) 191.
[84] M.C.J. Bradford, M.A. Vannice, Appl. Catal. A 142 (1996) 73.
[85] K.L. Yang, R.T. Yang, Carbon 24 (1986) 687.
[86] P.E. Nolan, D.C. Lynch, A.H. Cutler, Carbon 32 (1994) 477.
[87] S. Herreyre, P. Gadelle, Carbon 33 (1995) 234.
[88] D.W. McKee, in: P.L. Walker Jr., P.A. Thrower (Eds.), Chemistry and Physics of Carbon, Dekker, New York, 1981, p. 1.
[89] E. Boellaard, P.K. de Bokx, A.J.H.M. Kock, J.W. Geus, J. Catal. 96 (1985) 481.
[90] S. Takenaka, H. Ogihara, K. Otsuka, J. Catal. 208 (2002) 54.
[91] V.I. Zaikovskii, V.V. Chesnokov, R.A. Buyanov, Kinet. Catal. 40 (1999) 612.
[92] I. Alstrup, J. Catal. 109 (1988) 241.
[93] J.-W. Snoeck, G.F. Froment, M. Fowles, J. Catal. 169 (1997) 240.
[94] R.T. Yang, J.P. Chen, J. Catal. 115 (1989) 52.